Journal of Energy Storage 99 (2024) 113142

Contents lists available at ScienceDirect

Journal of Energy Storage

journal homepage: www.elsevier.com/locate/est

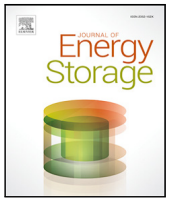

Research papers

A novel hybrid electrochemical equivalent circuit model for online battery management systems

Chengxi Cai, You Gong, Abbas Fotouhi, Daniel J. Auger *

Faculty of Engineering and Applied Sciences, Cranfield University, College Road, Cranfield, Bedfordshire, MK43 0AL, United Kingdom

ARTICLE INFO

Dataset link: https://doi.org/10.57996/cran.ceres-2597

Keywords:
Batteries
Online parameter estimation
State estimation
Simplified electrochemical model

ABSTRACT

Accurate battery modeling and parameter identification play pivotal roles in ensuring safety and reliability across the entire battery life cycle. Equivalent circuit models (ECM) are convenient but do not represent physical characteristics well; in contrast, electrochemical models with strong physical meaning are hard to parameterizing in an online setting. To address these challenges, this paper introduces a novel hybrid electrochemical Equivalent Circuit Model (eECM), which integrates electrochemical processes into an ECM, representing slow-dynamic internal processes with a simplified representation of solid- and liquid-phase diffusion; fast-dynamics are represented by ECM terms. The model is supported by an Adaptive Extended Kalman Filter (AEKF) to manage battery state changes and mitigate noise. To enhance parameter identification, a Fisher information matrix-enhanced Variable Forgetting Factor Recursive Least Squares (Fisher-VFFRLS) approach is employed, guided by the Cramér–Rao bound for identifying the most sensitive data points directly from the discharge cycle. Electrochemical parameters are determined via post-charging rest via a Genetic Algorithm (GA). The proposed methodology is validated on three dynamic cycles—DST, US06, and FUDS-demonstrates the effectiveness of the proposed eECM and parameter identification strategy, with maximum Root Mean Square Error (RMSE) for terminal voltage and State of Charge (SoC) estimation below 0.0076 and 0.0122, respectively.

1. Introduction

To date, Lithium-ion (Li-ion) batteries have emerged as a primary energy storage solution for Electric Vehicles (EVs) in terms of high energy density, excellent Coulombic efficiency, and long service life [1]. While the development of battery technology is at the heart of EVs, Battery Management Systems (BMSs) are equally vital to facilitate EV performance since the higher energy capacity, high power delivery and fast charging abilities of Li-ion battery systems impose high requirements on hazard protection and safety assurance [2]. In addition to managing charging/discharging safety, A BMS also needs optimal usage of batteries to improve energy efficiency. Accurately estimating the battery status online is prior required for the efficient implementation of BMS functions.

Battery modeling is a significant technology in EV applications, determining the feasibility and accuracy of battery real-time state-of-charge (SoC) estimation. Modeling approaches can be typically categorized into electrical Equivalent Circuit Model (ECM) and Electrochemical Model (EM). The ECM approach has been commonly applied in practice due to the mature parametric technology, acceptable accuracy under most operational conditions, and ease of implementation in microprocessors [3]. Such models are typically constructed by a voltage source, internal resistance and one or several resistor-capacitor (RC) pair(s) in a circuit, where the internal state of the battery is described by combining the characteristics exhibited by these circuit components [4].

However, the ECM presents poor performance under high C-rate conditions and edge SoC regions, limiting the potential to improve the estimation accuracy of batteries in EV applications [5]. Past studies [6,7] proposed the method that adds a Warburg impedance in the electric circuit to describe the low-frequency phase to improve model performance under high C-rate conditions. Correspondingly, a structure consisting of a parallel resistance and constant phase element circuit has been presented to simplify the Warburg impedance [8]. Nonetheless, parameterizing this fractional-order model requires Electrochemical Impedance Spectroscopy (EIS) tests under steady-state conditions (i.e., at a fixed SoC), which are challenging to apply in a real BMS [9]. Moreover, Considering long-term applying potentials, ECM struggle to account for battery degradation in terms of capacity and power fade, due to the lack of physical significance of the model parameters.

* Corresponding author.
E-mail address: d.j.auger@cranfield.ac.uk (D.J. Auger).

https://doi.org/10.1016/j.est.2024.113142
Received 7 May 2024; Received in revised form 10 July 2024; Accepted 25 July 2024
Available online 8 August 2024

In contrast, the EM approach is an excellent choice when accuracy is considered the most important performance [10]. This model provides an insightful description of the internal microscopic processes through several coupled Partial Differential Equations (PDEs), including electrochemical reaction kinetics, mass, heat transfer, etc. These physical representations allow more reliable and efficient observation of both the internal and external characteristics. Newman et al. pioneered the Pseudo-2-Dimensional model (P2D), which laid the foundation for numerous modeling studies [11–13]. This model can accurately describe most of the internal processes, e.g. mass and charge conservation, electrochemical kinetic, and output terminal voltage. The structure of this model is convenient for incorporating additional phenomena, such as side reactions for age evaluation [14] and thermal behaviors [15]. Nevertheless, coupled PDEs make solving P2D models a computational cost process, presenting a barrier to its real-time online application.

To decrease the computational cost of the P2D model, a reduced-order Single Particle Model (SPM) has been proposed to simplify the number of PDEs from several to a single. This model treats the electrode as two spatial domains that directly exchange Li-ion with each other and assume uniform current density in the electrolyte. With loss of the liquid phase diffusion dynamic, the high C-rate representation performance is sharply limited. To further enhance, the extension of the SPM approach with considerations of liquid phase diffusion [16,17] and thermal behavior [18] has been shown to achieve a performance that closely approximates the P2D model with a significant reduction in computational cost [12]. However, the procedure of spatially discretizing PDEs to Ordinary Differential Equations (ODEs) remains a computationally intensive task, so it cannot be implemented on microprocessors [19,20].

The concept of the extended ECM, which hybridizes the advantages of the ECM's simple structure and the EM's insightful internal process description, presents additional opportunities for improving accuracy and reducing complexity. The literature [21,22] have developed a phenomenological ECM that represents each internal reaction through independent electric circuit elements. This model consists of physics-based sub-circuits that govern individual species' phenomena. Thus, it could successfully reflect the internal battery performance characteristics such as concentrations, potentials, and overpotentials. However, this model's complex structure makes it challenging to parameterize and be used in EV microprocessors.

The ECM performs well in fast dynamic scenarios but is weak in slow dynamics, a limitation that can be addressed by incorporating elements from the EM. A promising approach to enhance model accuracy while maintaining low computational cost is to integrate diffusion processes into the ECM model, taking the slow dynamic into account. The kinetic behavior of the solid phase is highly nonlinear due to the phase-dependent lithium diffusivity and variations in lithium concentration gradients during operation.[23]. Inspired by the infinite difference method for SPM discretization, the solid diffusion process is represented by utilizing a series of differently weighted first-order inertial elements to describe the diffusion process. The OCV is then determined via a surface SoC [5,24,25]. Moreover, the omission of the liquid phase diffusion in online modeling limits model accuracy, particularly under high C-rate conditions. This becomes crucial in EVs applications where dynamic high-power requirements are frequently encountered in real-world environments. The latest design for high energy density electrodes emphasizes the advantage of large particle size of active material and thick electrode, making the influence of diffusion polarization become much more significant [26].

On the other hand, accurate model parameterization is essential for ensuring efficient and reliable state estimations and control facing the external environment and internal battery status change. Forgetting-Factor Recursive Least Square (FFRLS) is a widely adopted parameterization technology for online applications [27,28]. Owing to the advantage of online implementation, this technology is adopted in this article to estimate the battery parameters. However, FFRLS commonly grapples with numerical instability. Under conditions of insufficient excitation (e.g. constant low current when cruising), the parameter identification result suffers from numerical instability and sensor noise as a result of large parameter error covariance [29]. This phenomenon can lead to a failure to ensure convergence. Some modification methods focus on adjusting the forgetting factor according to the error [30] or condition number [29], but they lack insight into the inherent issue of insufficient excitation. Furthermore, the intricate nature of the ECM imposes additional constraints on the performance of FFRLS, especially in real-world scenarios characterized by random excitations that may occasionally be parameter-sensitive [31]. Because of the increasing parameter number of EM, the weak sensitivity becomes a much more severe problem for parameter identification [32,33].

In addition to physics-based state estimation technologies, many data-driven methods utilizing machine learning or deep learning are introduced for battery state estimation. SoC estimation is a typical time series prediction task, making it an excellent candidate for handling by long short-term memory (LSTM) networks [34] or transformer-based technologies [35]. Their powerful regression capabilities and flexible input structures enable fusion of multi health features for SoH estimation and RUL prediction [36,37]. Nevertheless, such black-box technologies still require further enhancement in terms of interpretability and computational cost for online application.

To address the aforementioned challenges, this study proposes an electrochemical and electrical equivalent circuit model (eECM) considering electrochemical properties, along with corresponding model parameter identification methods and observer design for online BMS application. The contributions of this study are as follows.

1. An enhanced eECM is proposed, integrating both solid-phase and liquid-phase diffusion into the Thevenin model. All diffusion processes are simplified to 1D diffusion processes and expressed in state-space format. Only two more electrochemical parameters, solid diffusion rate and liquid diffusion rate, are added.
2. An online parameter identification method is proposed to enable parameter updates throughout life cycles. The ECM parameters are identified using a Fisher information matrix-enhanced variable forgetting factor recursive least squares (Fisher-VFFRLS) method, which considers data sensitivities. The EM parameters are identified from the rest periods after charging cycles using a Genetic Algorithm (GA).
3. The EM elements are simplified into a state-space format and then integrated into the ECM. An Adaptive Extended Kalman Filter (AEKF) can, therefore, be applied to both the EM and ECM components for noise cancellation and SoC estimation.

The remainder of this paper is structured as follows: Section 2 will present the novel eECM development. Section 3 will detailed introduce the model parameter identification methods for ECM elements and EM parts. The verification results of the terminal voltage and SoC estimation via AEKF will be discussed in Section 4. Section 5 will conclude and explore the future potential of this work.

2. Electrochemical equivalent circuit model

A cell's dynamics are governed by electrochemical, chemical, and physical processes on different time scales. We proposed a novel eECM model to represent distinct time scale polarization with individual ECM or EM components, therefore separating their contributions to the terminal voltage. The overall schematic of eECM is shown in Fig. 1.a. In eECM, the characteristic frequencies (reciprocal of time constants) higher than 10 Hz are defined as a fast dynamic, described by ECM components. In contrast, the process lower than 10 Hz is addressed by EM parts. More specifically, the characteristic can be categorized into three segments via a typical EIS test [38–40]:

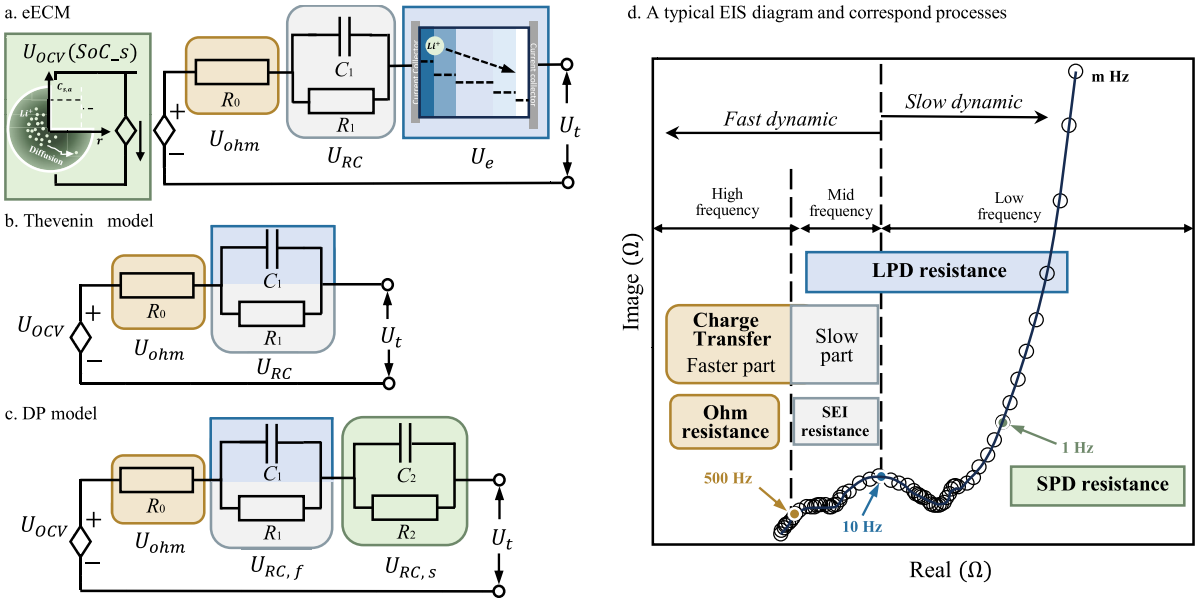

Fig. 1. a. Diagram of eECM structure b. Thevenin model c. DP model d. Typical EIS test and corresponding internal processes [38–40].

1. The high-frequency region (> 500 Hz) includes the Ohm polarization and the high-frequency part of the charge transfer polarization, denoted by U_{ohm} and marked in brown. This part is represented by the ECM part R_0.
2. The mid-frequency region between 10 Hz and 500 Hz encompasses the low-frequency parts of charge transfer resistance and SEI layer resistance. Their polarization is denoted as U_{RC} (marked as gray), represented by the ECM component $R_1//C_1$.
3. The low-frequency region, lower than 10 Hz, is described by EM components. This part comprises Solid Phase Diffusion (SPD) and Liquid Phase Diffusion (LPD). The SPD polarization is integrated into the voltage source, represented by U_{OCV} (marked in green). The LPD polarization (marked in blue) is expressed by U_e and connected in series to the circuit.

In contrast to the ECM model, the Thevenin model (shown in Fig. 1.b) accurately represents the high-frequency region with an internal resistance. Most fast-dynamic processes (mid frequency processes) are coupled with the only RC pair $R_1//C_1$, while the slow dynamic SPD cannot be involved [38]. Add one more RC pair $R_2//C_2$, the DP model (shown in Fig. 1.c) can separately express the low-frequency region for SPD. Therefore, the fast-dynamic and slow-dynamic processes are described by $U_{RC,f}$ and $U_{RC,s}$ separately. But model RC pair as SoC-dependence can only reflect the phase transition to the mean electrode level, the internal concentration gradient cannot be addressed, which lead error in latest thick electrode [38]. For the same reason, it cannot explain the hysteresis phenomenon caused by SPD. The thick electrode also limits the LPD speed, making it insufficient to be included in the mid-frequency region coupled within mid-frequency polarization via $R_1//C_1$. In terms of model parameter identification, adding an additional RC pair causes the model to become only locally identifiable. [41]. The indiscriminate addition of RC pairs increases the risk of overfitting and obscures the physical meanings of parameters [42].

The main limitation of the EM for online applications is the computational intensity of coupled PDEs (shown in Fig. 2.a). The model integrates mass and charge conservation in both the electrode and electrolyte, coupling a system of PDEs through the pore wall flux of Li-ions and charges, illustrating the intricacies of the electrode-electrolyte intercalation reaction via the Butler–Volmer (BV) equation. This model assumes homogeneity for most internal variables and introduces thick and porous material considerations through effective transport parameters, often employing the Bruggeman correlation [43]. However, since BV equations couple all PDEs, solving all processes simultaneously incurs high computational costs. Moreover, representing polarization at the cell level requires a large number of physical and geometric parameters. Most of these parameters have a weak correlation with the battery terminal voltage, making it challenging to identify the complete set of parameters [44].

In the proposed eECM, we adopt the easy parameter identification structure of the Thevenin model and keep the fast-dynamic part (> 10 Hz), which is well-proven and adequate in many academic and industry cases. The missing slow-dynamic polarization from SPD and LPD is governed by simplified EM elements. The 1D diffusion simplification decoupled them from BV equations and then converted all the PDEs to ODEs. Therefore, eECM can make a good compromise between the clear physical representation and computational cost.

2.1. Electrochemical components

From the electrochemical viewpoint, the diffusion process in a battery involves intercalation/deintercalation in the solid phase and movement in the liquid phase. The proposed simplification description of the diffusion process is derived from the P2D model. The U_{OCV} is determined by the potential difference between the cathode and anode surface, which is related to the surface Li-ion concentration. Besides, the Nernst equation also defines the liquid phase overpotential U_e by two surface electrolyte concentrations. Thus, in terms of a control-oriented model, the detailed distribution within the electrode and electrolyte is less critical compared to the surface concentration difference.

This study separates each electrode into surface and bulk control volume. Four control volumes are formed in the solid phase and five in the electrolyte phase (adding separator control volumes), as illustrated in Fig. 2.b. To simplify the diffusion process to one dimension, the current is assumed to be uniformly distributed on the electrode surface, and the pore-wall flux between the electrode and electrolyte is confined to the surface control volume. Conventional P2D and SPM models (shown in Fig. 2.a) treat the electrode as either multi or single spheres and consider radial Li-ion distribution. The calculation of internal distribution requires solving coupled PDEs, which is beyond the capability of current online BMS.

The surface concentration and its change rate are the points of interest on the macro scale. Hence, eECM assumes each control volume

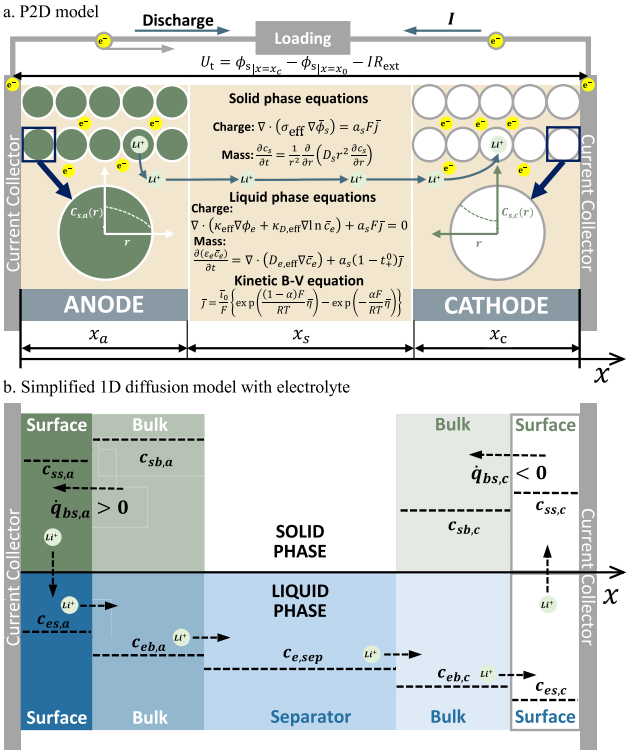

Fig. 2. a. Diagram of P2D model and SPM b. Simplified diffusion process at solid and liquid phase.

contains uniformly distributed Li-ions rather than calculating the detail distribution. Intuitively, the surface concentration change is caused by the applied current and Li-ions exchange with bulk volume. The diffusion rate is determined by the concentration gradient. In the bulk and separator control volume, the Li-ion concentration change solely depends on the diffusion led by the concentration gradient. The detailed derivation will be included in the liquid diffusion parts. Noticeably, this assumption can still address the phase transition phenomena, which significantly affect the overpotential during high C-rate operation scenarios. This function is critical to monitor battery behavior during fast charging and the high power response of EVs.

In this model, the charge current is considered positive. Fig. 2.b takes an example of a galvanostatic discharge scenario. The charge migrates from the anode to the cathode in the external circuit, while Li-ions move from the anode to the cathode in the interior. In the solid phase, Li-ions deintercalate from the active material into the electrolyte, decreasing concentration at the anode surface and increasing at the electrolyte surface. Simultaneously, at the cathode surface volume, Li-ions intercalate into the cathode from the electrolyte. Once a steady-state condition is reached, a constant concentration gradient arises within the electrolyte, facilitating Li-ion diffusion from the anode to the cathode.

2.1.1. Solid phase diffusion

Neglecting migration in the solid phases, the diffusion rate between surface and bulk $\dot{q}_{bs,i}$ is defined by Fick's first law:

$$\dot{q}_{bs,i} = \frac{1}{D_s}(c_{sb,i} - c_{ss,i}) \tag{1}$$

where D_s is the SPD rate, $c_{sb,i}$ and $c_{ss,i}$ represent the Li-ion concentration at the bulk and surface, which depend on the number of Li-ions and volume of each control volume:

$$c_{sb,i} = \frac{q_{sb,i}}{v_{sb,i}} \quad c_{ss,i} = \frac{q_{ss,i}}{v_{ss,i}} \tag{2}$$

$q_{ss,i}$ and $q_{sb,i}$ is the number of Li-ions in solid phase surface ($v_{ss,i}$) and solid phase bulk ($v_{sb,i}$), i refers to the anode or cathode. The applied current (I) induces the change of Li-ion concentration at the surface area. In the anode, the surface electrode concentrate is lower than bulk, thus $\dot{q}_{bs,a} > 0$. The change in the number of Li-ions can, therefore, be expressed as:

$$\dot{q}_{ss,a} = I + \dot{q}_{bs,a} \tag{3}$$

Similarly, the result cathode surface Li-ion concentration is higher than bulk. Therefore, $\dot{q}_{bs,c} < 0$. The actual diffusion direction is from surface to bulk. Again, the change in the number of Li-ions is:

$$\dot{q}_{ss,c} = -I + \dot{q}_{bs,c} \tag{4}$$

Eq. (3) and (4) denote a large current will lead to a sharp change in the electrode surface, causing a large concentration gradient. When the applied current is removed, the diffusion will continue until a uniform concentration, which accounts for SoC and voltage recovery. The total amount of Li-ions within electrodes can be expressed as:

$$q^{max} = q_a + q_c \tag{5}$$

$$q_a = q_{sb,a} + q_{ss,a} \quad q_c = q_{sb,c} + q_{ss,c} \tag{6}$$

q_a and q_c represent the amount of Li-ions at the anode and cathode. q^{max} represent the maximum amount of Li-ions, which is linked to the battery capacity C:

$$q^{max} = 3600 \cdot C \tag{7}$$

The electrode surface SoC and bulk SoC are defined as the fraction of the current number of Li-ions to its maximum value.

$$SoC_{ss,i} = \frac{q_{ss,i}}{q^{max}_{ss,i}} = \frac{c_{ss,i}}{c^{max}_{ss,i}} \tag{8}$$

$$SoC_{sb,i} = \frac{q_{sb,i}}{q^{max}_{sb,i}} = \frac{c_{sb,i}}{c^{max}_{sb,i}} \tag{9}$$

where

$$q^{max}_{ss,i} = q^{max}\frac{v_{ss,i}}{v_i} \quad q^{max}_{sb,i} = q^{max}\frac{v_{sb,i}}{v_i} \tag{10}$$

v_i denotes the electrode volume. The SPD rate is assumed to be equal at the cathode and anode. In Eq. (10), the maximum Li-ions at the surface ($q^{max}_{ss,i}$) and bulk ($q^{max}_{sb,i}$) volume is a constant value in each electrode. The summary of Li-ions at surface and bulk volume is also a consent value, and the SoC relationship can, therefore, be expressed as:

$$SoC_{ss,a} = 1 - SoC_{ss,c} \quad SoC_{sb,a} = 1 - SoC_{sb,c} \tag{11}$$

Finally, the anode SoC can represent the cell SoC as follows:

$$SoC_s = SoC_{ss,a} \quad SoC_b = SoC_{sb,a} \tag{12}$$

2.1.2. State space format of solid-phase diffusion

Determining the OCV in an electrochemical system can be challenging, especially in online applications where installing a three-electrode battery is not feasible. In such cases, an ECM is usually used to estimate the OCV by utilizing the mean SoC and an SoC-OCV lookup table. However, this method cannot accurately describe the concentration polarization caused by the diffusion process. According to the Nernst equation, the OCV is determined by Li-ion concentration at the surface, equivalent to surface SoC (SoC_s). The bulk Li-ions concentration, i.e. bulk SoC (SoC_b), represents the overall battery status related to the ECM parameters and battery SoC. The representation of solid-phase diffusion polarization and non-linear OCV is shown in Fig. 3. The SoC_s will lead or delay to the SoC_b during the charge or discharge process, respectively. This approach offers several unique benefits:

a. SPD Expression: OCV identified through the OCV-SOC table by SoC_s will diverge from the bulk value. This divergence describes the influence of diffusion overpotential on the OCV, which enhances the battery dynamic representation of OCV.

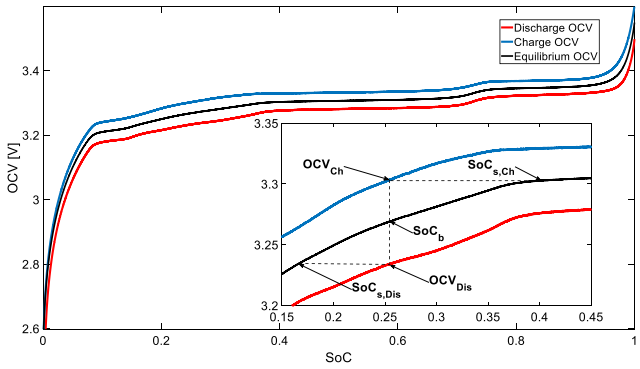

Fig. 3. The representation of solid-phase overpotential and OCV non-linear.

b. OCV Hysteresis Explanation: The lead or delay of bulk SoC during charge or discharge conditions results in various OCV curves. These curves provide insights into OCV hysteresis.

c. Realistic SoC Representation: At edge SoC regions, the surface SoC representation may yield values below 0 or above 1. This indicates that the surface electrode is overcharged or over-discharged, a hazardous condition that should be avoided in real-world applications. This additional information contributes to safety monitoring and state-of-power estimation.

As previously mentioned, the anode surface and bulk concentration are chosen as state variables to determine the surface and bulk SoC.

$$\begin{cases} \dot{c}_{ss,a} = [D_s(c_{ss,a} - c_{sb,a}) + I]/v_{ss} \\ \dot{c}_{sb,a} = [-D_s(c_{ss,a} - c_{sb,a})]/v_{sb} \end{cases} \tag{13}$$

Rewrite Eq. (13) to the matrix form:

$$\begin{bmatrix} \dot{c}_{ss,a} \\ \dot{c}_{sb,a} \end{bmatrix} = \begin{bmatrix} \frac{D_s}{v_{ss}} & -\frac{D_s}{v_{ss}} \\ -\frac{D_s}{v_{sb}} & \frac{D_s}{v_{sb}} \end{bmatrix} \begin{bmatrix} c_{ss,a} \\ c_{sb,a} \end{bmatrix} + \begin{bmatrix} \frac{1}{v_{ss}} \\ 0 \end{bmatrix} I \tag{14}$$

It is clear that the concentration change at the surface volume is directly linked to the applied current and the exchange of Li-ions between the bulk volume. The bulk concentration change depends only on the concentration gradient with the surface volume, which diffusion speed solely related to the concentration gradient and solid state diffusion ratio. The cell SoC and OCV are calculated based on the solid-phase states by:

$$\begin{cases} SoC_s = \dfrac{c_{ss,a} v_b}{q^{max}_{ss,a}} \\ SoC_b = \dfrac{c_{sb,a} v_s}{q^{max}_{sb,a}} \\ OCV = U_{OCV}(SoC_s) \end{cases} \tag{15}$$

2.1.3. Liquid phase diffusion

Under steady-state conditions, the electrolyte concentration is uniformly distributed throughout the entire electrolyte. When an external current excitation is applied, for example, a discharge current. Li-ions undergo deintercalation from the electrode active material, transferring to the electrolyte at the anode. Meanwhile, Li-ions intercalate into the electrode at the cathode. The Li-ion exchange between liquid and solid phase is assumed to be concentrated in the surface volume; a potential difference is built between the two electrodes' surfaces due to the increasing concentration on the anode side and the decreasing concentration on the cathode side. In general, the distribution of electrolyte concentration can be characterized by [45]:

$$\frac{\partial}{\partial t}\varepsilon_e c_e = \frac{\partial}{\partial x}\left(D_e^{\text{eff}} \frac{\partial}{\partial x} c_e\right) + (1 - t_+)\frac{j_f}{F} \tag{16}$$

where t_+ is the electrolyte transfer number and F is Faraday constant, j_f is the volumetric current density. D_e^{eff} is the efficient electrode diffusion rate. The various micro-structures of two electrodes induce different diffusion resistances, which can be evaluated by the porosity ε_e and Brugg coefficient as:

$$D_e^{\text{eff}} = D_e \varepsilon_i^{\text{brugg}} \tag{17}$$

More specifically, three distinct equations for the anode, cathode, and separator are employed to describe the detailed electrolyte concentration distributions:

$$c_e(x,t) = \begin{cases} c_{e,a}(x,t) & 0 \le x \le x_a \\ c_{e,s}(x,t) & x_a \le x \le x_a + x_s \\ c_{e,c}(x,t) & x_a + x_s \le x \le L \end{cases} \tag{18}$$

where x_a and x_b is the thickness of anode and separator region, L is the total length of the battery. Integrating three equations, the amount of Li-ions at each part can be expressed:

$$\begin{cases} Q_{e,a}(t) = \varepsilon_{e,a} \int_0^{x_a} c_{e,a}(x,t)dx \\ Q_{e,s}(t) = \varepsilon_{e,s} \int_{x_a}^{x_a+x_s} c_{e,s}\left(x,t\right)dx \\ Q_{e,c}(t) = \varepsilon_{e,c} \int_{x_a+x_s}^{L} c_{e,c}\left(x,t\right)dx \end{cases} \tag{19}$$

Consequently, Eq. (16) for each region can be written as:

$$\begin{cases} \frac{\partial}{\partial t}\varepsilon_{e,a} c_{e,a} = \frac{\partial}{\partial x}\left(D_{e,a}^{\text{eff}} \frac{\partial}{\partial x} c_{e,a}\right) + (1 - t_+)\frac{j_f}{F} & (0 \le x \le x_a) \\ \frac{\partial}{\partial t}\varepsilon_{e,s} c_{e,s} = \frac{\partial}{\partial x}\left(D_{e,s}^{\text{eff}} \frac{\partial}{\partial x} c_{e,s}\right) & (x_a \le x \le x_a + x_s) \\ \frac{\partial}{\partial t}\varepsilon_{e,c} c_{e,c} = \frac{\partial}{\partial x}\left(D_{e,c}^{\text{eff}} \frac{\partial}{\partial x} c_{e,c}\right) + \left(1 - t_+\right)\frac{j_f}{F} & (x_a + x_s \le x \le L) \end{cases} \tag{20}$$

The boundary conditions for solving these PDEs include three groups:

1. No mass flow at two edge sides of electrode:

$$\left.\frac{\partial c_{e,a}}{\partial x}\right|_{x=0} = 0, \quad \left.\frac{\partial c_{e,c}}{\partial x}\right|_{x=L} = 0 \tag{21}$$

2. Continuous concentration and diffusion flux at anode-separator interface

$$c_{e,a}\left(x_a,t\right) = c_{e,s}\left(x_a,t\right) \tag{22}$$

$$D_{e,a}^{\text{eff}} \left.\frac{\partial c_{e,a}}{\partial x}\right|_{x=x_a} = D_{e,s}^{\text{eff}} \left.\frac{\partial c_{e,s}}{\partial x}\right|_{x=x_a} \tag{23}$$

3. Continuous concentration and diffusion flux at cathode-separator interface

$$c_{e,c}\left(x_a + x_s,t\right) = c_{e,s}\left(x_a + x_s,t\right) \tag{24}$$

$$D_{e,c}^{\text{eff}} \left.\frac{\partial c_{e,c}}{\partial x}\right|_{x=x_a+x_s} = D_{e,s}^{\text{eff}} \left.\frac{\partial c_{e,s}}{\partial x}\right|_{x=x_a+x_s} \tag{25}$$

4. Li-ions conservation

$$Q_{e,a}(t) + Q_{e,s}(t) + Q_{e,c}(t) = c_0 L \tag{26}$$

Taking into account charge conservation at each electrode, The relationship between the volumetric current density j_f and pore wall flux j_n can be expressed by:

$$j_n = \frac{j_f}{a_s F} \tag{27}$$

where a_s is the interfacial surface area related to the electrode microstructure. Assume the current distribution inside the whale electrode is uniform where the pore-wall flux for any particles is the same. Thus, the local volumetric current density can be represented by the average volumetric current density following spatial integrals:

$$\int_0^{x_a} j_{f,a}(x,t)dx = \frac{I}{A} = \bar{j}_{f,a} x_a \tag{28}$$

$$\int_{x_a+x_s}^{L} j_{f,c}\left(x,t\right)dx = -\frac{I}{A} = \bar{j}_{f,c}x_c \tag{29}$$

where A is the cell electrode plate area. Combine Eq. – and boundary conditions, the PDEs for the concentrations distributions are converted to the ODEs that describe the change of the total amount of Li-ions:

$$\begin{cases} \frac{d}{dt}Q_{e,a}(t) = (1-t_+)\frac{I}{F} + D_{e,a}^{\text{eff}}\left.\frac{\partial c_{e,c}(x,t)}{\partial x}\right|_{x=x_a} \\ \frac{d}{dt}Q_{e,s}(t) = D_{e,s}^{\text{eff}}\left.\frac{\partial c_{e,s}(x,t)}{\partial x}\right|_{x=x_a+Ls} - D_{e,s}^{\text{eff}}\left.\frac{\partial c_{e,s}(x,t)}{\partial x}\right|_{x=x_a} \\ \frac{d}{dt}Q_{e,c}(t) = -(1-t_+)\frac{I}{F} - D_{e,c}^{\text{eff}}\left.\frac{\partial c_{e,c}(x,t)}{\partial x}\right|_{x=x_a+x_s} \end{cases} \tag{30}$$

2.1.4. State space format of liquid-phase diffusion

$$\begin{bmatrix} \dot{c}_{es,a} \\ \dot{c}_{eb,a} \\ \dot{c}_{e,s} \\ \dot{c}_{eb,c} \\ \dot{c}_{es,c} \end{bmatrix} = \begin{bmatrix} \frac{-D\varepsilon_a^{1.5}}{v_{es}} & \frac{D\varepsilon_a^{1.5}}{v_{es}} & 0 & 0 & 0 \\ \frac{D\varepsilon_a^{1.5}}{v_{eb}} & -2\frac{D\varepsilon_a^{1.5}}{v_{eb}} & \frac{D\varepsilon_a^{1.5}}{v_{eb}} & 0 & 0 \\ 0 & \frac{-D\varepsilon_a^{1.5}}{v_s} & \frac{-D\varepsilon_a^{1.5}-D\varepsilon_c^{1.5}}{v_s} & \frac{D\varepsilon_a^{1.5}}{v_s} & 0 \\ 0 & 0 & \frac{D\varepsilon_c^{1.5}}{v_{eb}} & -2\frac{D\varepsilon_c^{1.5}}{v_{eb}} & \frac{D\varepsilon_c^{1.5}}{v_{eb}} \\ 0 & 0 & 0 & \frac{D\varepsilon_c^{1.5}}{v_{es}} & \frac{-D\varepsilon_c^{1.5}}{v_{es}} \end{bmatrix} \begin{bmatrix} c_{es,a} \\ c_{eb,a} \\ c_{e,s} \\ c_{eb,c} \\ c_{es,c} \end{bmatrix} + \begin{bmatrix} -\frac{1-t^+}{v_{es}} \\ 0 \\ 0 \\ 0 \\ \frac{1-t^+}{v_{es}} \end{bmatrix} I \tag{31}$$

Based on the previous equations, it is evident that the variation in Li-ion concentration within the electrode region is influenced by two distinct factors. Taking the anode as an example, the first component of Li-ion change arises from deintercalation, wherein Li-ions are released from the active material. This process is directly proportional to the applied current, owing to the principle of charge conservation. The second component of the equation accounts for the diffusion of Li-ions from the separator to the anode, driven by the concentration gradient. Importantly, the aforementioned relationship holds true for any conditions, as the previous derivations do not assume any specific electrolyte concentration distribution. In previous studies, many studies suggested Padé approximation, parabolic functions, and asymptotic reduction Leading-order approximation methods to determine the internal Li-ion distribution [13,19,33]. However, all the existing methods for battery modeling require updating the concentration distribution after every time step, which can be computationally expensive for online applications.

For control-oriented battery modeling, calculating the diffusion polarization of the liquid phase requires only knowledge of surface area concentration and its changes. The diffusion rate between control volumes only influenced by each concentration follows Fick's first law. Therefore, this model used a similar method for the solid phase by dividing the entire battery into five control volumes and assuming a uniform distribution where diffusion only occurs at the connected surface. The surface control volumes are aligned to the solid phase surface control volumes where the pore-wall flux exists. Thus the Eq. (30) can be simplified to:

$$\begin{cases} \dot{c}_{es,a} = [-(1-t^+)I - D\varepsilon_a^{1.5}(c_{es,a} - c_{eb,a})]/v_{es} \\ \dot{c}_{eb,a} = D[\varepsilon_a^{1.5}(c_{es,a} - c_{eb,a}) - \varepsilon_a^{1.5}(c_{eb,a} - c_{e,s})]/v_{eb} \\ \dot{c}_{e,s} = D[\varepsilon_a^{1.5}(c_{eb,a} - c_{e,s}) - \varepsilon_c^{1.5}(c_{e,s} - c_{eb,c})]/v_s \\ \dot{c}_{eb,c} = D[\varepsilon_c^{1.5}(c_{e,s} - c_{eb,c}) - \varepsilon_c^{1.5}(c_{eb,c} - c_{es,c})]/v_{eb} \\ \dot{c}_{es,c} = [(1-t^+)I - D\varepsilon_a^{1.5}(c_{eb,a} - c_{es,a})]/v_{es} \end{cases} \tag{32}$$

The state-space matrix form of LPD is listed in Eq. (31) (above). It indicates that the applied current only affects the edge side of the electrode, creating concentration gradient, and inducing Li-ion diffusion throughout the entire liquid phase. The LPD polarization can be calculated by the surface Li-ion concentration via the Nernst equation [45]:

$$U_e = (1-t^+)\frac{2RT}{F}\ln\left(\frac{c_{es,a}}{c_{es,c}}\right) \tag{33}$$

where, T is temperature, R is universal gas constant.

Table 1
Summary Of polarization equations.

U_{OCV}	SoC	U_e	U_{RC}	U_{ohm}
Eq. (14) & (15)	Eq. (14) & (15)	Eq. (31) & (33)	Eq. (34)	Eq. (35)

2.2. Equivalent circuit model components

The rest of eECM is a standard Thevenin model where the only state variable is the voltage of the RC pair:

$$\dot{U}_{RC} = -\frac{1}{R_1C_1}U_{RC} + \frac{1}{C_1}I \tag{34}$$

The ohmic polarization is regarded as a transient variable. The voltage drop (U_{ohm}) changes quickly in response to its charge or discharge current and follows:

$$U_{ohm} = R_0 I \tag{35}$$

2.3. Summary

In summary, the eECM combines EM and ECM components to describe various internal processes separately and write them into the state-space format. Table 1 summarized the equations for all polarization-related components.

The final output equations can, therefore be written as:

$$U_t = U_{OCV}(SoC_s) + U_{ohm} + U_{RC} + U_e \tag{36}$$

3. Model parameter identification

The ECM and EM components separately represent internal processes of different time scales. Identifying all the model parameters simultaneously is a time-consuming and imprecise process, especially in a real-time application. Therefore, model parameter identification should be considered separately to fully utilize the available data. This study identifies the ECM model parameters from the dynamic discharge cycle. In contrast, EM model parameters are determined from the charge cycle, especially the rest period after a Constant Voltage (CV) charge. The applied current is removed during this period, and the internal diffusion process causes all voltage changes. Even though all polarization simultaneously influences the terminal voltage response, the distinct differences in time constants make it reasonable to assume that the influence of the diffusion process can be neglected during ECM model parameter identification in the discharge process.

3.1. ECM model parameter identification

Before discussing the techniques for identifying model parameters, it is essential to consider two critical aspects: structural identifiability and parameter sensitivity. Structural identifiability is a property that allows inferring unknown parameters by measuring the output over time, independent of the quantity or quality of the observed data. Parameter sensitivity emphasizes the quality of excitation for parameter identification. The objective is to ensure that the model is uniquely identified, and that the parameter identification process uses the most data rich excitation points.

For the first one, the ECM part in this study adopts the Thevenin model, which is related to structural identifiability [41]. The second

objective focuses on guaranteeing that the most appropriate data are selected for the identification of the model parameters. This reduces the risk of numerical instability in RLS algorithms. In this study, a Fisher information matrix is utilized to assess the data richness of the excitation. The Cramér–Rao bound is adopted as a data sufficiency index to cross-validate the data richness among cycles. In our previous work, this method has been verified in a single dynamic discharge cycle, demonstrating its effectiveness [46]. However, there is no guarantee that sensitive points exist in a single cycle. This study uses three dynamic cycles to allow the model parameters to evolve among the cycles based on the data richness.

In terms of parameter identification, the FFRLS algorithm is the most commonly used method for both online and offline usage. The sudden and steady conditions always appear alternately in real-world EVs. With increasing recursions, correcting new data becomes challenging, and the algorithm loses its tracking and correction ability, posing a risk of divergence for FFRLS algorithms. Therefore, a variable forgetting factor is employed to handle dynamic conditions, ensuring robust enhancement. In comparison to conventional FFRLS, a variable forgetting factor recursive least squares (VFFRLS) can dynamically adjust the forgetting factor value based on the error, responsively determines the extent of discarding or reserving old data in an online and adaptive manner. However, VFFRLS still does not inherently solve the risk of insufficient excitation. Therefore, a Fisher-VFFRLS is proposed to actively select the data richest points for online parameter identification.

Fig. 4 introduces the structure of the Fisher-VFFRLS algorithms. $x_{i,SoC}$ represents the model parameters in a specific SoC region, and the subscript i means different parameters. The $C_{SoC(x_i)}$ indicated the historical lowest Cramér–Rao bound, which indicates the data richness. Depending on the operation time scale, the algorithm can be divided into three time scales:

1. Time step: VFFRLS operates simultaneously with data collection at each time step.
2. 1% SoC level: Fisher information matrix selects the most sensitive points at each 1% change in SoC and records the sensitive index value
3. Cycles level: The determination and evolution of look-up tables will progress through cycles.

Model parameter changes occur gradually according to the battery SoC. The resolution of the look-up table is set to 1% change in SoC to guarantee a smooth transition between states while avoiding compromise of system stability and robustness. Thus, a 100-point look-up table is formed. At each SoC segment, the historical lowest Cramér–Rao bound and corresponding model parameters are stored, representing the best estimation obtained thus far. In subsequent cycles, whenever a 1% SoC change occurs, the newly calculated local data-richest point will be compared with a historical data-rich point. If a lower Cramér–Rao bound is achieved, then update the model parameters and record the latest Cramér–Rao bound as the new historical data-richest point. Otherwise, the previous Cramér–Rao bound and previous model parameters remain the most data-rich estimates, which will be preserved for the next cycle.

3.1.1. VFFRLS

A recursive expression for parameter identification can be written as discrete form by:

$$U_{t,k} = \boldsymbol{\Phi}_k \boldsymbol{\Theta}_k \tag{37}$$

where,

$$\boldsymbol{\Phi}_k = [U_{t,k-1} \quad I_k \quad I_{k-1} \quad 1]$$
$$\boldsymbol{\Theta}_k = [\theta_1 \quad \theta_2 \quad \theta_3 \quad U_{OCV}(1-\theta_1)]^T$$

Here, $\boldsymbol{\Phi}_k$ bring in the input data, and $\boldsymbol{\Theta}_k$ indicate the lumped model parameter matrix include intermediate parameters θ_1, θ_2, and θ_3.

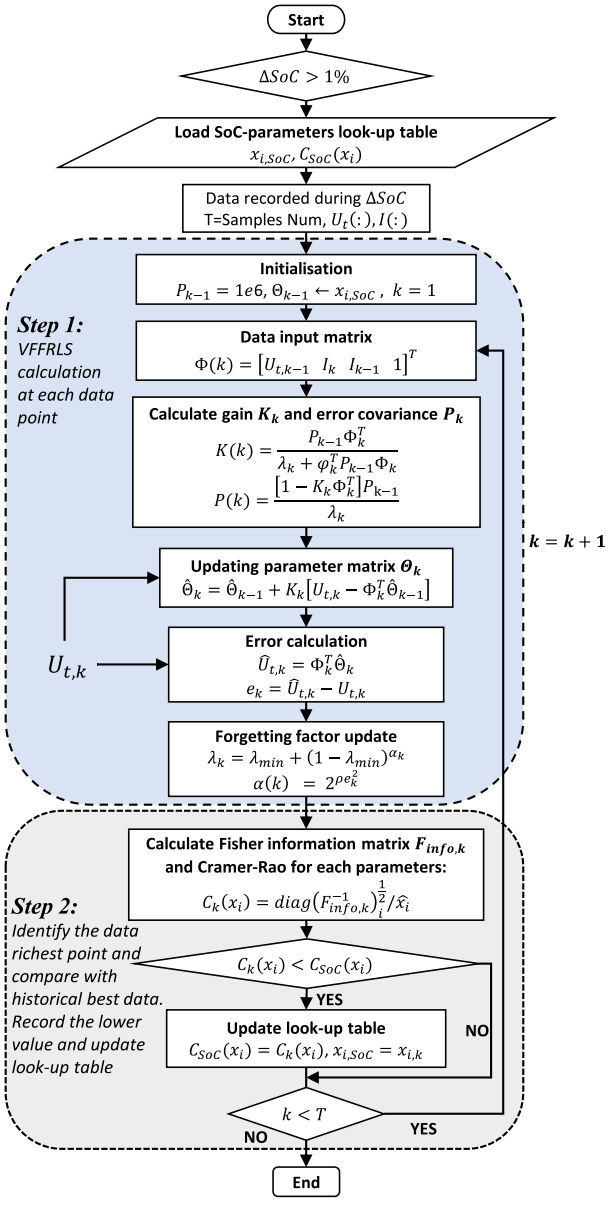

Fig. 4. An implementation flowchart of Fisher-VFFRLS algorithm.

In each SoC segment, the data is injected as time series: $[U_{t,0}, \boldsymbol{\Phi}_0]$, $[U_{t,1}, \boldsymbol{\Phi}_1]$...$[U_{t,k}, \boldsymbol{\Phi}_k]$, VFFRLS then finds the best model parameter estimation by minimizing the least squares error of the terminal voltage through the cost function:

$$\boldsymbol{\Theta} = \arg\min_{\boldsymbol{\Theta}} \frac{1}{k}\sum_{t=1}^{k}(\hat{U}_t(t|\boldsymbol{\Theta}) - U_t)^2 \tag{38}$$

Once the optimized value of $\boldsymbol{\Theta}$ is achieved, the model parameters (R_0, R_1, C_1 and U_{OCV}) can be derived by Eq. (39):

$$\begin{cases} R_0 = \dfrac{\theta_3 - \theta_2}{1 + \theta_1} \\ R_1 = -2\dfrac{\theta_1\theta_2 + \theta_3}{1 - \theta_1^2} \\ C_1 = -\dfrac{T(1 + \theta_1^2)}{4(\theta_1\theta_2 + \theta_3)} \\ U_{OCV} = \dfrac{\theta_4}{1 - \theta_1} \end{cases} \tag{39}$$

Many previous works have already addressed the FFRLS procedure in depth [28]; most equations are presented in Fig. 4 Step 1. Where K_k is the gain vector, and P_k is the covariance matrix. e represents the terminal voltage prediction error. λ is the forgetting factor between 0 to 1. A smaller value assigns less contribution of previous samples to the covariance matrix, making it more sensitive to the latest sample, and vice versa. The stability of the RLS can be affected by the error. In practice, the parameter change is also influenced by environmental conditions and sensor errors. For stable parameter tracking, reducing the forgetting factor when the error is large is crucial. If an error is small, the parameter needs less change and therefore a larger forgetting factor is required [47,48]. The details of the VFFRLS algorithm are listed in Fig. 4 Step 1, the unique part is this final procedure that tune the forgetting factor based on the prediction error. The fixed parameters λ_{min} and ρ are set at 0.8 and 10,000, respectively.

3.1.2. Fisher information matrix

RLS identifies the model parameters based on the output signals of the battery model and measured data. The information contained in the output directly determines the quality of the identification results. The Fisher information matrix evaluates the derivative of the output with respect to each model parameter, providing a means to assess the adequacy of output data [49–51]. The Fisher information matrix is expressed as

$$F_{\text{info},k+1} = \frac{1}{\sigma_y^2}\left(\frac{\partial Y}{\partial(x|\Theta_{k+1})}\right)^T\left(\frac{\partial Y}{\partial(x|\Theta_{k+1})}\right) \tag{40}$$

where σ_y^2 is the variance of the terminal voltage measurement error assumed to be Gaussian. Y is the system output (here is terminal voltage), and x is the model parameters matrix, $[R_0, R_1, C_1, U_{OCV}]$, that need to be identified. Here, Y can be derived from Eq. (36):

$$U_{t,k+1} = U_{OCV,k} - I_{k+1}R_0 - \mathrm{e}^{\frac{-T}{\tau}}U_{1,k} - I_k R_1(1-\mathrm{e}^{\frac{-T}{\tau}}) \tag{41}$$

Thus, at time $k+1$

$$\frac{\partial Y}{\partial(x|\Theta_k)} = \begin{bmatrix}\frac{\partial U_t}{\partial R_0} & \frac{\partial U_t}{\partial R_1} & \frac{\partial U_t}{\partial C_1} & \frac{\partial U_t}{\partial U_{OCV}}\end{bmatrix}^T \tag{42}$$

where,

$$\begin{cases}\dfrac{\partial U_t}{\partial R_0} = -I_{k+1}\\ \dfrac{\partial U_t}{\partial R_1} = I_k\left(\mathrm{e}^{-\frac{T}{\hat{\tau}}}-1\right) + \dfrac{I_k T\,\mathrm{e}^{-\frac{T}{\hat{\tau}}}}{\hat{C}_1\hat{R}_1} - \dfrac{T\,U_{1,k}\,\mathrm{e}^{-\frac{T}{\hat{\tau}}}}{\hat{C}_1\hat{R}_1^2}\\ \dfrac{\partial U_t}{\partial C_1} = -\dfrac{T\,\mathrm{e}^{-\frac{T}{\hat{\tau}}}\left(U_1 - I_k\hat{R}_1\right)}{\hat{C}_1^2\hat{R}_1}\\ \dfrac{\partial U_t}{\partial U_{OCV}} = 1\end{cases} \tag{43}$$

Here, $\hat{R}_1$, $\hat{C}_1$ means estimated value from VFFRLS. $\hat{\tau}$ is calculated time constant for RC pair equal to $\hat{R}_1 \cdot \hat{C}_1$. The Cramér–Rao bound uses a judgment index to represent the minimum variance of estimation error extracted from the Fisher information matrix.[50,52]. It establishes the lowest estimation covariance of an unbiased estimator via the inverse of the Fisher information matrix:

$$\mathrm{cov}_{\text{est}}(x_i) \geq \bar{\sigma}^2(x_i) = \mathrm{diag}(F_{\text{info}}^{-1})_i \tag{44}$$

Here, the $\sigma^2(x_i)$ is the Cramér–Rao bound for the ith model parameters which is represented by the ith diagonal value of the F_{info}^{-1}. A lower value indicates a better identification result, meaning that the corresponding excitation can be considered as a satisfactory input. In this study, the normalized Cramér–Rao bounds are employed as data sufficient index for each model parameter, which is expressed as:

$$C(x_i) = \bar{\sigma}(x_i) = \mathrm{diag}(F_{\text{info}}^{-1})_i^{\frac{1}{2}}/\hat{x} \tag{45}$$

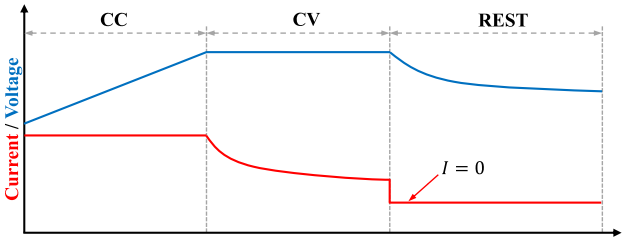

Fig. 5. Diagram of a typical CC-CV charge pattern with rest.

It is important to note that the sensitivity for OCV remains constant at a value of 1. To calculate OCV sensitivity, multiply all diagonal elements of Cramér–Rao bounds to obtain an overall sensitivity value that is used to represent U_{OCV} sensitivity:

$$C(U_{OCV}) = \prod \bar{\sigma}(x_i) \tag{46}$$

3.2. EM model parameter identification

The sensitivity of identifying model parameters in EM is challenging due to the inclusion of over thirty parameters in a P2D model [53,54]. For the electrochemical elements of our control-oriented model, diffusion-related model parameters are simplified to two parameters: the solid-phase and liquid-phase diffusion coefficient, which dominate the diffusion process. Moreover, these two parameters are strongly sensitive to terminal voltage response and surface potential (U_{OCV}) [55,56].

The electrochemical elements primarily represent slow dynamic and high C-rate polarization in the eECM model. Considering real-world applications, diffusion-induced polarization is relatively insignificant within dynamic excitations during discharge. In contrast, the charging process is more consistent, providing enough time to capture over-potential caused by diffusion. In a typical charging cycle (as shown in Fig. 5), the charging process begins with one or multiple constant current (CC) phases, followed by a constant voltage (CV) charge when the terminal voltage reaches the cut-off voltage. Once the charging cycle is complete, removing the current excitation, the terminal voltage will gradually drop until it reaches equilibrium. The rest of the process is purely caused by the diffusion process; therefore, it was selected for the EM parameters identification. The diffusion overpotential is a highly nonlinear process affected by not only the different solid and LPD rates, but also the internal concentration gradient. In this study, the EM parameters are identified via a GA algorithm. The accumulated terminal voltage error of eECM is selected as the fitness function for optimization.

$$\begin{aligned}\text{fitness} = &\\ &W_1\cdot\sum_{t_0}^{t_1} abs\left(U_t-\hat{U}_t\right) + W_2\cdot\sum_{t_1}^{t_2} abs\left(U_t-\hat{U}_t\right) +\\ &\cdots + W_n\cdot\sum_{t_{n-1}}^{t_n} abs\left(U_t-\hat{U}_t\right)\\ &= \sum_{t_0}^{t_n} W(t)\cdot abs\left(U_t(t)-\hat{U}_t\right)\end{aligned} \tag{47}$$

where U_t and $\hat{U}_t$ are the measured and simulated terminal voltage. This fitness function represents the sum of the absolute error at each time interval. The coefficient W_t is used to weight the contribution of each time interval during the optimization process. The optimization mainly depends on the rest period but includes part of the CV process to determine the initial conditions of the rest period. A lower weight is given to the CV part, while a higher weight is assigned to the rest process.

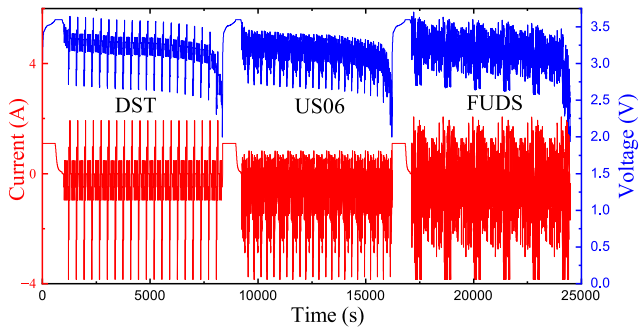

Fig. 6. Raw data of DST, US06 and FUDS cycles.

Table 2
eECM electrochemical parameters.

Parameters	Value
Identified parameters	
D_s	8×10^{-8} m^3/s
D_e	5×10^{-6} m^3/s
Selected parameters	
Ce	1000 mol/m^3
F	96485.3329 sA/mol
t_+	0.4
R	8.3144 J/K/mol
T	298 K
v_s	2×10^{-6} m^3
v_b	2×10^{-5} m^3
ϵ_a	0.45
ϵ_c	0.3
$brugg$	1.5

4. Model validation

This study utilized data from an A123 battery tested in the Center for Advanced Life Cycle Engineering (CALCE) of the University of Maryland, including three dynamic cycles - DST, US06, and FUDS. The cell used is LiFePO4, with a rated capacity of 1100 mAh. During the battery test, the cell is firstly charged to 100% SoC and allowed to rest until equilibrium is reached. It is then discharged with different duty cycles. Once the battery approaches the 0% SoC, it is rested again before repeating the charging process. Raw data are shown in Fig. 6. The identification and verification of model parameters are performed using Matlab/Simulink 2023a. The identification of model parameters involved two steps: first, ECM elements are identified from dynamic discharge data, and then two diffusion-related EM parameters are determined from the rest data after CC charge. Finally, the identified model parameters are validated through the estimation of the terminal voltage and SoC.

4.1. Model parameter identification

The results of identifying the ECM parameter include the ohmic resistance, RC pair parameters, and OCV. Identification results are shown in Fig. 7 . The blue and red lines show the model parameters identified from one and all three cycles. As far as we know, the model parameter identified from DST has the best performance. Therefore, it is adopted to represent the performance of model parameters identified from one cycle. Compared to conventional VFFRLS (shown in black), our proposed method produces a smoother curve that is very much subject to a basic understanding that the model parameters change slowly and smoothly. The reason why conventional VFFRLS fails is due to the lack of rich information excitation, which makes it sensitive to excitation dynamics. Additionally, there is no guarantee that sufficient excitation will be obtained in one cycle. Hence, the proposed model receives the most sensitive data among cycles. This is especially crucial for identifying the OCV data, which is one of the most essential characteristics of the battery cell. However, the sensitivity of the OCV is a constant value of 1 and much larger than other parameters (usually 1e15-1e-20), making it almost insensitive to the input signals. The accurate estimation heavily relies on the overall data richest points. Identification results show a significant improvement in OCV estimation at the edge of SoC and less error compared to the separate OCV test under 1/20 C (shown in the magenta line). The EM model parameters used for the verification are shown in Table 2. The two core diffusion-related model parameters identified from the rest period via GA are 8×10^{-8} and 5×10^{-6} m^3/s. Other EM parameters related to the cell structure are selected from the literature.

Taking into account the online computational cost, the method involves generating a 100-point look-up table that covers one cycle of data. On an i7-9700 CPU, it takes approximately 0.1383 s, 0.1264 s, and 0.1268 s for DST, US06, and FUDS tests, respectively. This time already encompasses all costs related to VFFRLS, Fisher information matrices, and GA. Calculating the Fisher information matrix for the 1% SoC segment ranges from 0.001 s to 0.008 s, depending on the data length, which is considerably less than the 1 s sample time. Furthermore, these algorithms update the look-up table every 1% SoC, ensuring ample time for online calculation.

Table 3
Terminal Voltage Estimation RMSE.

Models	DST	US06	FUDS
ECM (DST)	0.0141	0.0113	0.0125
ECM (All)	0.0135	0.0106	0.0121
eECM	0.0086	0.0066	0.0074

4.2. Terminal voltage verification

Fig. 8 shows the results of terminal voltage verification. The black line represents the measured terminal voltage, while the blue and red lines represent the terminal voltage simulation values from the ECM and eECM. The terminal voltage response can be better followed when the diffusion process is applied. This is because a high current excitation causes a rapid concentration change at both the electrode and electrolyte surface volume, and the resulting diffusion-induced overvoltage cannot be neglected. Furthermore, the influence of high C-rate excitation would not be eliminated in a short time period in the following time steps. The time constant of the RC pair is around 2–3 s, and the influence of slow-dynamic diffusion can last much longer than this value. This explains why eECM performs better when the battery is under high current excitation and during the following time steps. The RMSE results are listed in Table 3. For each cycle, the eECM significantly outperforms the conventional ECM. Comparison of the parameters identified from a single DST model and three cycles is also included. This indicates that the proposed model parameter identification methods can be improved by involving multi-cycles to improve accuracy. The US06 test resulted in the best estimate of terminal voltage with an RMSE of 0.0066 V; the largest RMSE was still lower than 0.0086 V.

4.3. SoC estimation results

SoC estimation is a core function of BMS in EVs. The proposed model needs to be able to perform accurately in real-world scenarios where the noise from sensors cannot be ignored. This study injected artificial white noise into lab-collected data to test its functionality. The actual data used for SoC estimation is presented in Fig. 9, where the yellow line represents the raw data, and the red and blue lines denote the current and voltage data used for the estimation, respectively. The

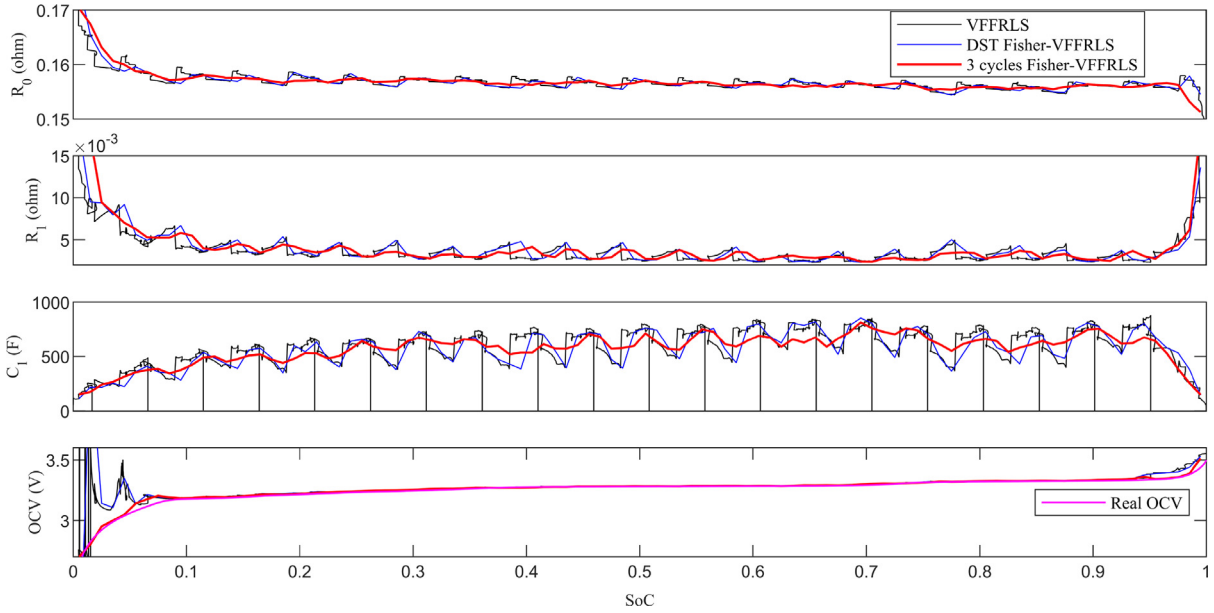

Fig. 7. Parameter identification results. (For interpretation of the references to color in this figure legend, the reader is referred to the web version of this article.)

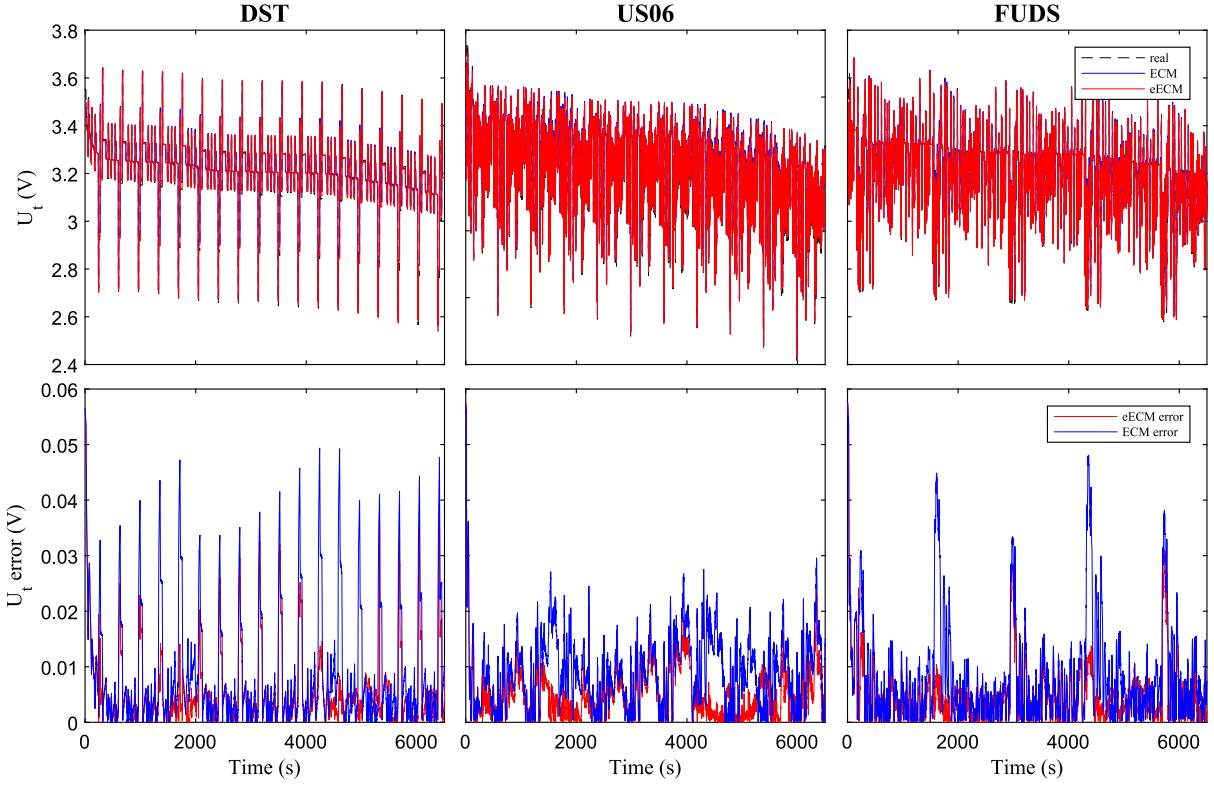

Fig. 8. Terminal voltage estimation result in DST, US06 and FUDS cycles.

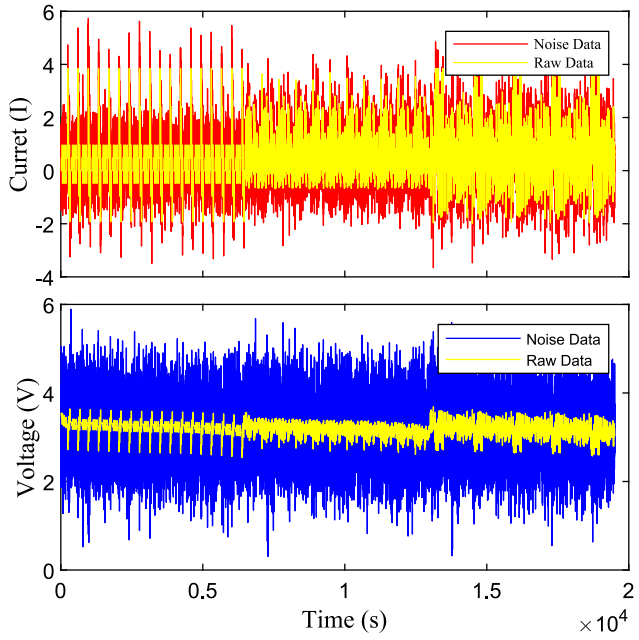

Fig. 9. Data used for SoC estimation with added noise.

AEKF algorithms are applied to both ECM and eECM using noise data. Implementing AEKF on ECM has been well explored in many previous studies [28]. In eECM, the state of SPD is adopted as a state function by Eq. (14). The discrete form for AEKF can be expressed as:

$$\mathbf{x_k} = \mathbf{F}\,\mathbf{x_{k-1}} + \mathbf{Q}_k$$

$$\mathbf{x} = \begin{bmatrix} \mathbf{c}_{ss,a} \\ \mathbf{c}_{sb,a} \end{bmatrix}$$

$$\mathbf{F} = \begin{bmatrix} \frac{v_s}{v_s+1} + \frac{\sigma}{v_s+1} & \frac{v_s}{v_b(v_s+1)} - \frac{v_s\sigma}{v_b(v_s+1)} \\ \frac{v_b}{v_s+1} - \frac{v_b\sigma}{v_s+1} & \frac{1}{v_s+1} + \frac{v_s\sigma}{v_s+1} \end{bmatrix} \tag{48}$$

where $\sigma = \mathrm{e}^{\frac{T(D_s+D_s v_s)}{v_s}}$

where **F** is state transition matrix, and **Q** is the process noise. The ECM parameters are from the identified look-up tables. As the parameters change between two time steps can be neglected, the state equation can be treated as linear. In order to linearize the SoC-OCV equation in the measurement equation, the OCV is fitted to a seven-order polynomial function of SoC and consequently applies the Taylor expansion. Therefore, the measurement equation can be expressed as:

$$\mathbf{z}_k = \mathbf{H}\,\mathbf{x_k} - U_{ohm} - U_{RC} - U_e + \mathbf{R}_k$$

$$\mathbf{z} = U_t \qquad \mathbf{H} = \begin{bmatrix} \frac{d\,U_{OCV}}{d\,SoC} & \frac{v_b}{q_{ss,a}^{max}} \\ 0 \end{bmatrix} \tag{49}$$

H is the measurement model matrix and **R** is the measurement noise. The detail of the AEKF algorithm is presented in Algorithm 1. In a real-world application, the statistic characteristic of $\mathbf{Q}_k$ and $\mathbf{R}_k$ is not a prior. The innovation sequence is used to estimate and update iteratively following Step 5. Where N_k is the innovation covariance matrix calculated from innovation covariance matrix e, the sequence length M is set as 50.

In this eECM, the definition of SoC is represented separately by surface SoC (SoC_s) and bulk SoC (SoC_b), each influencing the OCV and the parameters of ECM independently. Precisely, SoC_s captures the dynamic surface polarization associated with diffusion-induced overvoltage, while SoC_b reflects a relatively stable internal concentration

Algorithm 1 AEKF for SoC estimation

Input: $\hat{\mathbf{x}}_{k-1}^{+}$ $\mathbf{P}_{x,k-1}^{+}$ $\mathbf{R}_{k-1}$ $\mathbf{Q}_{k-1}$

1: Prior prediction
$\hat{\mathbf{x}}_k^{-} = f(\mathbf{x}_{k-1}, u_{k-1})$ *(Eq. (14))*
2: Covariance update
$\mathbf{P}_{x,k}^{-} = \mathbf{F}_{k-1}\mathbf{P}_{x,k-1}^{+}\mathbf{F}_{k-1}^{T} + \mathbf{Q}_{k-1}$
3: Predict system output and error calculation
$\hat{\mathbf{z}}_k = h(\hat{\mathbf{x}}_k^{-}, u_k)$ *(Eq. (36))*
$e_k = \mathbf{z}_k - \hat{\mathbf{z}}_k$
4: Kalman gain ($\mathbf{L}_k$) calculation
$\mathbf{L}_k = \mathbf{P}_{x,k}^{-}\mathbf{H}_k^{T}[\mathbf{H}_k\mathbf{P}_{x,k}^{-}\mathbf{H}_k^{T} + \mathbf{R}_{k-1}]$
5: Adaptive noise matrix
$N_k = \frac{1}{M}\sum_{k-M+1}^{k} e_i e_i^{T}$
$\begin{cases} \mathbf{R}_k = N_k - N_k\mathbf{P}_{x,k}^{-}N_k^{T} \\ \mathbf{Q}_k = N_k\mathbf{L}_k N_k^{T} \end{cases}$
6: State estimation update
$\hat{\mathbf{x}}_k^{+} = \hat{\mathbf{x}}_k^{-} + \mathbf{L}_k \cdot e_k$
7: State covariance ($\mathbf{P}_{x,k}$) update
$\mathbf{P}_{x,k}^{+} = (\mathbf{I} - \mathbf{L}_k\mathbf{H}_k)\cdot\mathbf{P}_{x,k}^{-}$

Output: $\hat{\mathbf{x}}_k^{+}$ $\mathbf{P}_{x,k}^{+}$ $\mathbf{R}_k$ $\mathbf{Q}_k$

Table 4
SoC Estimation RMSE.

Models	DST	US06	FUDS
ECM (DST)	0.0172	0.0175	0.0174
ECM (All)	0.0136	0.0137	0.0142
eECM SoC_s	0.0222	0.0177	0.0197
eECM SoC_b	0.0120	0.0117	0.0122

condition. Therefore, SoC_b aligns with the conventional SoC definition, indicating the average charge distribution within the battery.

This study compares the SoC_s estimation result with raw data to verify the noise cancellation ability of eECM and AEKF. The estimation results are presented in Fig. 10. The black line is the eECM with raw data, and the red line is the eECM with noise data and AEKF. The AEKF guaranteed a RMSE lower than 0.02. Capacity values adopt the rated value, and the dynamic test cannot reach 0% SoC due to the lower cut-off voltage limitation. In this testing condition, the end SoC does not reach 0, but the final peak of the DST test pushes the surface SoC below zero. This indicates that the surface electrode is partly over-discharged, which is an unrecognized hazard in conventional control methods.

The SoC_b is compared with real SoC calculated through Coulomb counting methods using raw data. The ECM with AEKF is also adopted for comparison. The results and errors are depicted in Fig. 11, where the bulk SoC is in the red line, the ECM SoC is in the blue line, and the real SoC is in the black line. The battery performance of eECM can also be explained via the diffusion process. The current applied to the current collector is directly applied to the electrode surface layer and then permeates to bulk volume. In another world, the current could not directly influence the real SoC, thus leading to errors in the ECM model. In order to further prove the accuracy of the proposed Fisher-VFFRLS algorithm, the parameters from the DST cycle with AEKF are also included for SoC estimation comparison. The RMSE result is shown in Table 4. The online SoC estimation based on eECM SoC_b can efficiently limit the error below 0.0122, which shows that the eECM and AEKF can introduce a reliable monitoring ability in online applications such as EVs.

4.4. Summary

Integrating the SPD and LPD processes, eECM provides a clearer description of internal electrochemical reactions with significant physical implications and enhances state estimation performance. Firstly,

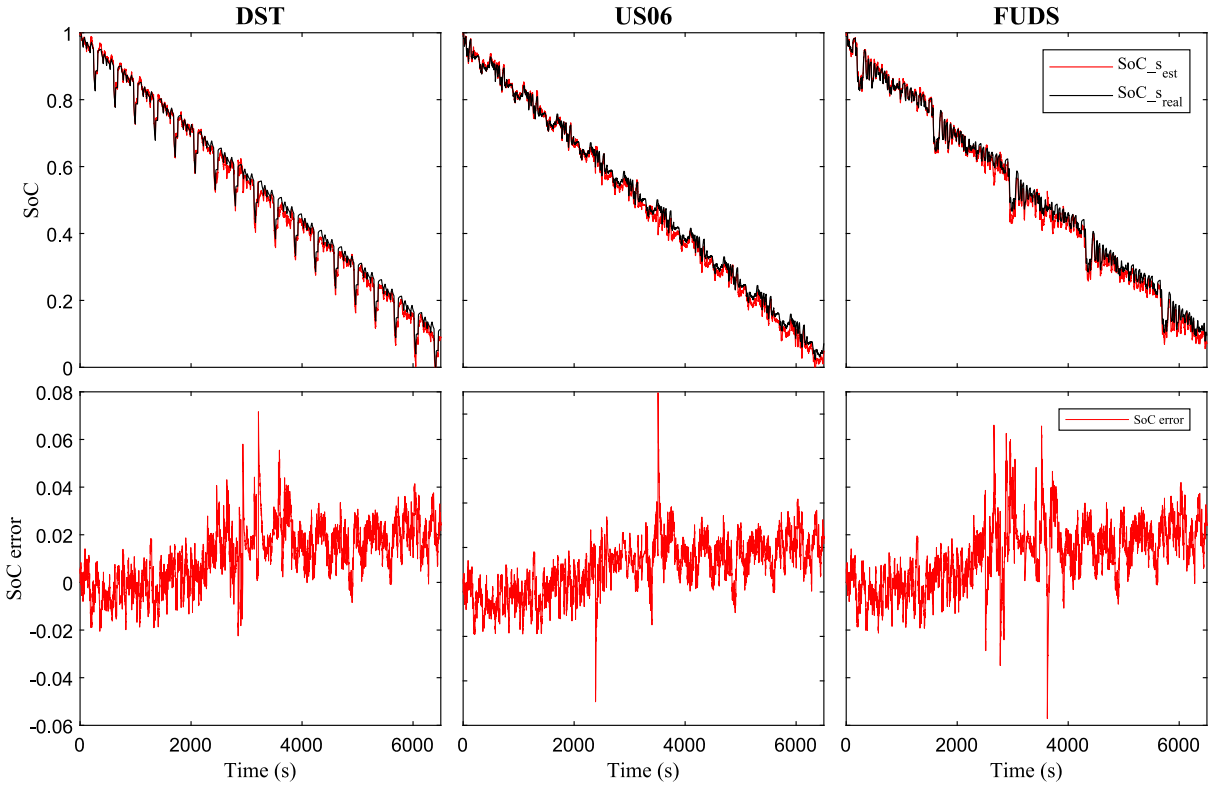

Fig. 10. Surface SoC estimation result in DST, US06 and FUDS cycles.

terminal voltage estimation accuracy improves by more than 36% compared to ECM across all dynamic tests, particularly benefiting from enhanced prediction following high-current operations and polarization at edge SoC region. Secondly, by treating bulk SoC to represent battery SoC, the eECM demonstrates substantial performance improvements across all SoC regions. Finally, eECM enables separate monitoring of surface and bulk SoC, facilitating the identification of local overcharge/overdischarge conditions that are not captured by ECM, which assumes electrode homogeneity throughout.

5. Conclusion

This paper introduces a modeling framework that integrates the electrochemical process into the conventional Thevenin model while maintaining the simplicity of parameterization and implementation inherent in the ECM structure. Previous studies have demonstrated the advantages of integrating the electrochemical process into the ECM model, and this study extends these findings by introducing the liquid-phase diffusion process to enable high C-rate and edge SoC usage. More importantly, this study provides an in-depth description of the corresponding internal processes based on their frequency response speed, effectively distinguishing between slow and fast dynamics. This differentiation enables online parameter identification capabilities. The proposed Fisher-VFFRLS method is applied to three driving cycles: DST, US06, and FUDS. The maximum RMSE for terminal voltage and SoC is demonstrated to be lower than 0.0086 and 0.0122, respectively.

Owing to its state-space format and full online parameterization capability, this model is promising for use in control applications within an online BMS onboard EVs. This work emphasizes its suitability for online operation, acknowledging that it is primarily simulation-based. Future work will focus on conducting hardware-in-the-loop tests to validate the methodology in real-world scenarios. The detailed description of internal processes provides additional opportunities for advanced control strategies aimed at optimizing power delivery, mitigating potential hazards, ensuring long-term usage, and predicting remaining useful life. Our future work will focus on exploring these additional functionalities to leverage the potential of the proposed eECM.

CRediT authorship contribution statement

Chengxi Cai: Writing – original draft, Visualization, Validation, Software, Resources, Project administration, Methodology, Investigation, Formal analysis, Data curation, Conceptualization. **You Gong:** Writing – review & editing. **Abbas Fotouhi:** Writing – review & editing, Supervision. **Daniel J. Auger:** Writing – review & editing, Supervision.

Declaration of competing interest

The authors declare that they have no known competing financial interests or personal relationships that could have appeared to influence the work reported in this paper.

Data availability

Data supporting this study are openly available from CERES at https://doi.org/10.57996/cran.ceres-2597.

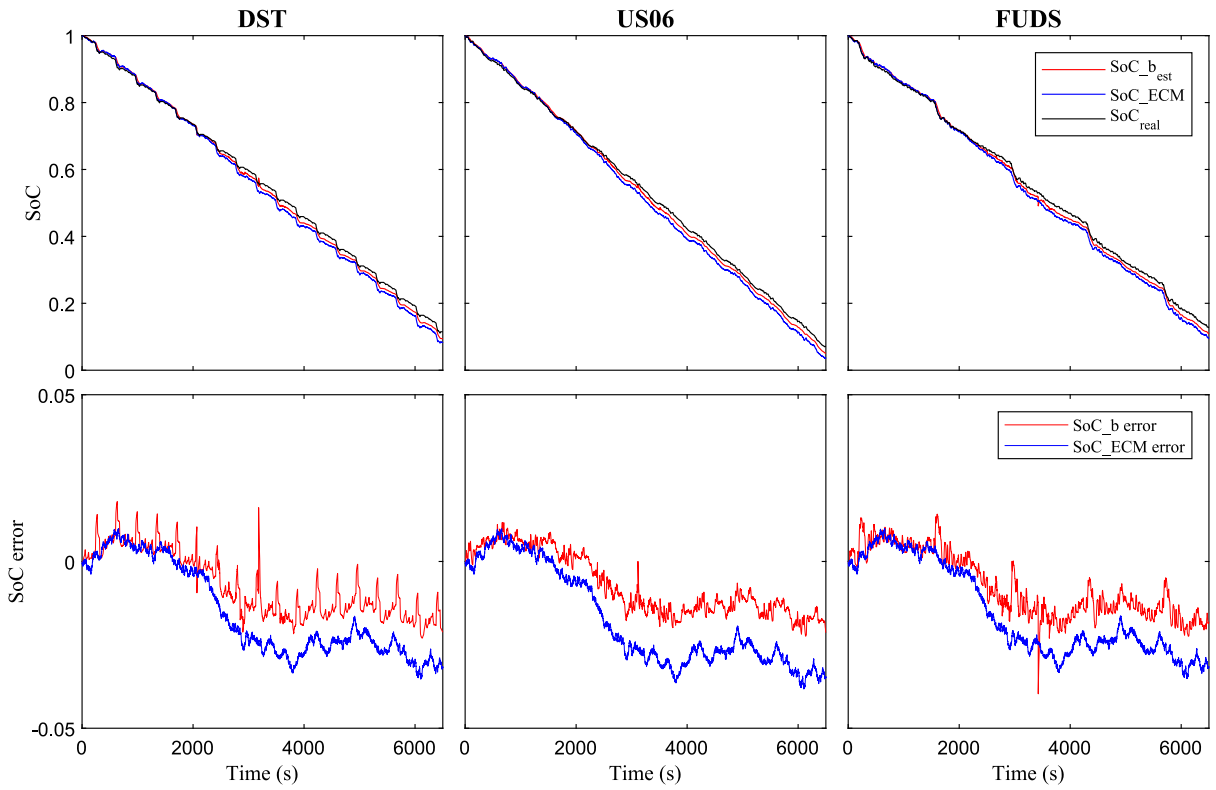

Fig. 11. Bulk SoC estimation result and ECM with EKF result in DST, US06 and FUDS cycles.

References

[1] Xinhai Yuan, Fuxiang Ma, Linqing Zuo, Jing Wang, Nengfei Yu, Yuhui Chen, Yusong Zhu, Qinghong Huang, Rudolf Holze, Yuping Wu, et al., Latest advances in high-voltage and high-energy-density aqueous rechargeable batteries, Electrochem. Energy Rev. 4 (2021) 1–34.

[2] Yujie Wang, Jiaqiang Tian, Zhendong Sun, Li Wang, Ruilong Xu, Mince Li, Zonghai Chen, A comprehensive review of battery modeling and state estimation approaches for advanced battery management systems, Renew. Sustain. Energy Rev. 131 (2020) 110015.

[3] Jinhao Meng, Guangzhao Luo, Mattia Ricco, Maciej Swierczynski, Daniel-Ioan Stroe, Remus Teodorescu, Overview of lithium-ion battery modeling methods for state-of-charge estimation in electrical vehicles, Appl. Sci. 8 (5) (2018) 659.

[4] Shunli Wang, Carlos Fernandez, Yu Chunmei, Yongcun Fan, Cao Wen, Daniel-Ioan Stroe, Zonghai Chen, Battery System Modeling, Elsevier, 2021.

[5] Yuejiu Zheng, Wenkai Gao, Xuebing Han, Minggao Ouyang, Languang Lu, Dongxu Guo, An accurate parameters extraction method for a novel on-board battery model considering electrochemical properties, J. Energy Storage 24 (2019) 100745.

[6] Hao Mu, Rui Xiong, Hongfei Zheng, Yuhua Chang, Zeyu Chen, A novel fractional order model based state-of-charge estimation method for lithium-ion battery, Appl. Energy 207 (2017) 384–393.

[7] Christian Fleischer, Wladislaw Waag, Hans-Martin Heyn, Dirk Uwe Sauer, On-line adaptive battery impedance parameter and state estimation considering physical principles in reduced order equivalent circuit battery models: Part 1. Requirements, critical review of methods and modeling, J. Power Sources 260 (2014) 276–291.

[8] Jufeng Yang, Wenxin Huang, Bing Xia, Chris Mi, The improved open-circuit voltage characterization test using active polarization voltage reduction method, Appl. Energy 237 (2019) 682–694.

[9] Nina Meddings, Marco Heinrich, Frédéric Overney, Jong-Sook Lee, Vanesa Ruiz, Emilio Napolitano, Steffen Seitz, Gareth Hinds, Rinaldo Raccichini, Miran Gaberšček, et al., Application of electrochemical impedance spectroscopy to commercial Li-ion cells: A review, J. Power Sources 480 (2020) 228742.

[10] Abbas Fotouhi, Daniel J. Auger, Karsten Propp, Stefano Longo, Mark Wild, A review on electric vehicle battery modelling: From Lithium-ion toward Lithium–Sulphur, Renew. Sustain. Energy Rev. 56 (2016) 1008–1021.

[11] John Newman, William Tiedemann, Porous-electrode theory with battery applications, AIChE J. 21 (1) (1975) 25–41.

[12] Ferran Brosa Planella, Muhammad Sheikh, W. Dhammika Widanage, Systematic derivation and validation of a reduced thermal-electrochemical model for lithium-ion batteries using asymptotic methods, Electrochim. Acta 388 (2021) 138524.

[13] Ali Jokar, Barzin Rajabloo, Martin Désilets, Marcel Lacroix, Review of simplified Pseudo-two-Dimensional models of lithium-ion batteries, J. Power Sources 327 (2016) 44–55.

[14] Andrea Lamorgese, Roberto Mauri, Bernardo Tellini, Electrochemical-thermal P2D aging model of a LiCoO2/graphite cell: Capacity fade simulations, J. Energy Storage 20 (2018) 289–297.

[15] Billy Wu, Vladimir Yufit, Monica Marinescu, Gregory J. Offer, Ricardo F. Martinez-Botas, Nigel P. Brandon, Coupled thermal–electrochemical modelling of uneven heat generation in lithium-ion battery packs, J. Power Sources 243 (2013) 544–554.

[16] Saeed Khaleghi Rahimian, Sean Rayman, Ralph E. White, Extension of physics-based single particle model for higher charge–discharge rates, J. Power Sources 224 (2013) 180–194.

[17] Ferran Brosa Planella, W. Dhammika Widanage, A single particle model with electrolyte and side reactions for degradation of lithium-ion batteries, Appl. Math. Model. 121 (2023) 586–610.

[18] Changbeom Hong, Hyeonwoo Cho, Daeki Hong, Se-Kyu Oh, Yeonsoo Kim, An improved thermal single particle model and parameter estimation for high-capacity battery cell, Electrochim. Acta 439 (2023) 141638.

[19] Aldo Romero-Becerril, Luis Alvarez-Icaza, Comparison of discretization methods applied to the single-particle model of lithium-ion batteries, J. Power Sources 196 (23) (2011) 10267–10279.

[20] Kandler A. Smith, Christopher D. Rahn, Chao-Yang Wang, Control oriented 1D electrochemical model of lithium ion battery, Energy Convers. Manage. 48 (9) (2007) 2565–2578.

[21] Yu Merla, Billy Wu, Vladimir Yufit, Ricardo F Martinez-Botas, Gregory J Offer, An easy-to-parameterise physics-informed battery model and its application towards lithium-ion battery cell design, diagnosis, and degradation, J. Power Sources 384 (2018) 66–79.

[22] Marie-Therese Von Srbik, Monica Marinescu, Ricardo F. Martinez-Botas, Gregory J. Offer, A physically meaningful equivalent circuit network model of a lithium-ion battery accounting for local electrochemical and thermal behaviour, variable double layer capacitance and degradation, J. Power Sources 325 (2016) 171–184.

[23] Maria Angeles Cabanero, Nicola Boaretto, Manuel Röder, Jana Müller, Josef Kallo, Arnulf Latz, Direct determination of diffusion coefficients in commercial li-ion batteries, J. Electrochem. Soc. 165 (5) (2018) A847.
[24] Minggao Ouyang, Guangming Liu, Languang Lu, Jianqiu Li, Xuebing Han, Enhancing the estimation accuracy in low state-of-charge area: A novel onboard battery model through surface state of charge determination, J. Power Sources 270 (2014) 221–237.
[25] Xuebing Han, Minggao Ouyang, Languang Lu, Jianqiu Li, Simplification of physics-based electrochemical model for lithium ion battery on electric vehicle. Part I: Diffusion simplification and single particle model, J. Power Sources 278 (2015) 802–813.
[26] Pengcheng Zhu, Peter R. Slater, Emma Kendrick, Insights into architecture, design and manufacture of electrodes for lithium-ion batteries, Mater. Des. (2022) 111208.
[27] Xiaosong Hu, Fengchun Sun, Yuan Zou, Huei Peng, Online estimation of an electric vehicle lithium-ion battery using recursive least squares with forgetting, in: Proceedings of the 2011 American Control Conference, IEEE, 2011, pp. 935–940.
[28] Hongwen He, Rui Xiong, Hongqiang Guo, Online estimation of model parameters and state-of-charge of LiFePO4 batteries in electric vehicles, Appl. Energy 89 (1) (2012) 413–420.
[29] Minho Kim, Kwangrae Kim, Soohee Han, Reliable online parameter identification of Li-ion batteries in battery management systems using the condition number of the error covariance matrix, IEEE Access 8 (2020) 189106–189114.
[30] Xiangdong Sun, Jingrun Ji, Biying Ren, Chenxue Xie, Dan Yan, Adaptive forgetting factor recursive least square algorithm for online identification of equivalent circuit model parameters of a lithium-ion battery, Energies 12 (12) (2019) 2242.
[31] Thomas R. B. Grandjean, Andrew McGordon, Paul A. Jennings, Structural identifiability of equivalent circuit models for Li-ion batteries, Energies 10 (1) (2017) 90.
[32] Moritz Streb, Malin Andersson, Verena Löfqvist Klass, Matilda Klett, Mikael Johansson, Göran Lindbergh, Investigating re-parametrization of electrochemical model-based battery management using real-world driving data, eTransportation 16 (2023) 100231.
[33] Kailong Liu, Yizhao Gao, Chong Zhu, Kang Li, Minrui Fei, Chen Peng, Xi Zhang, Qing-Long Han, Electrochemical modeling and parameterization towards control-oriented management of lithium-ion batteries, Control Eng. Pract. 124 (2022) 105176.
[34] Shunli Wang, Paul Takyi-Aninakwa, Siyu Jin, Chunmei Yu, Carlos Fernandez, Daniel-Ioan Stroe, An improved feedforward-long short-term memory modeling method for the whole-life-cycle state of charge prediction of lithium-ion batteries considering current-voltage-temperature variation, Energy 254 (2022) 124224.
[35] Zhengyi Bao, Jiahao Nie, Huipin Lin, Kejie Gao, Zhiwei He, Mingyu Gao, TTSNet: State-of-charge estimation of Li-ion battery in electrical vehicles with temporal transformer-based sequence network, IEEE Trans. Veh. Technol. (2024).
[36] Shunli Wang, Yongcun Fan, Siyu Jin, Paul Takyi-Aninakwa, Carlos Fernandez, Improved anti-noise adaptive long short-term memory neural network modeling for the robust remaining useful life prediction of lithium-ion batteries, Reliab. Eng. Syst. Saf. 230 (2023) 108920.
[37] Mingqiang Lin, Yuqiang You, Jinhao Meng, Wei Wang, Ji Wu, Daniel-Ioan Stroe, Lithium-ion batteries SOH estimation with multimodal multilinear feature fusion, IEEE Trans. Energy Convers. 38 (4) (2023) 2959–2968.
[38] Dongxu Guo, Geng Yang, Xuning Feng, Xuebing Han, Languang Lu, Minggao Ouyang, Physics-based fractional-order model with simplified solid phase diffusion of lithium-ion battery, J. Energy Storage 30 (2020) 101404.
[39] Jun Huang, Zhe Li, Hao Ge, Jianbo Zhang, Analytical solution to the impedance of electrode/electrolyte interface in lithium-ion batteries, J. Electrochem. Soc. 162 (13) (2015) A7037.
[40] Haifeng Dai, Tianjiao Xu, Letao Zhu, Xuezhe Wei, Zechang Sun, Adaptive model parameter identification for large capacity Li-ion batteries on separated time scales, Appl. Energy 184 (2016) 119–131.
[41] Seyed Mohammad Mahdi Alavi, Adam Mahdi, Stephen J. Payne, David A. Howey, Identifiability of generalized randles circuit models, IEEE Trans. Control Syst. Technol. 25 (6) (2016) 2112–2120.
[42] Meijuan Yu, Yan Li, Igor Podlubny, Fengjun Gong, Yue Sun, Qi Zhang, Yunlong Shang, Bin Duan, Chenghui Zhang, Fractional-order modeling of lithium-ion batteries using additive noise assisted modeling and correlative information criterion, J. Adv. Res. 25 (2020) 49–56.
[43] Bernhard Tjaden, Samuel J. Cooper, Daniel J.L. Brett, Denis Kramer, Paul R. Shearing, On the origin and application of the bruggeman correlation for analysing transport phenomena in electrochemical systems, Curr. Opin. Chem. Eng. 12 (2016) 44–51.
[44] Emil Namor, Dimitri Torregrossa, Rachid Cherkaoui, Mario Paolone, Parameter identification of a lithium-ion cell single-particle model through non-invasive testing, J. Energy Storage 12 (2017) 138–148.
[45] E. Prada, D. Di Domenico, Y. Creff, J. Bernard, Valérie Sauvant-Moynot, F. Huet, Simplified electrochemical and thermal model of LiFePO4-graphite li-ion batteries for fast charge applications, J. Electrochem. Soc. 159 (9) (2012) A1508.
[46] Chengxi Cai, Daniel J. Auger, Suresh Perinpanayagam, Enhanced online identification of battery models exploiting data richness, in: 2023 IEEE International Conference on Electrical Systems for Aircraft, Railway, Ship Propulsion and Road Vehicles & International Transportation Electrification Conference, ESARS-ITEC, IEEE, 2023, pp. 1–6.
[47] Constantin Paleologu, Jacob Benesty, Silviu Ciochina, A robust variable forgetting factor recursive least-squares algorithm for system identification, IEEE Signal Process. Lett. 15 (2008) 597–600.
[48] Zizhou Lao, Bizhong Xia, Wei Wang, Wei Sun, Yongzhi Lai, Mingwang Wang, A novel method for lithium-ion battery online parameter identification based on variable forgetting factor recursive least squares, Energies 11 (6) (2018) 1358.
[49] Michael J. Rothenberger, Joel Anstrom, Sean Brennan, Hosam K. Fathy, Maximizing parameter identifiability of an equivalent-circuit battery model using optimal periodic input shaping, in: Dynamic Systems and Control Conference, Vol. 46186, American Society of Mechanical Engineers, 2014, p. V001T19A004.
[50] Xinfan Lin, Anna G. Stefanopoulou, Analytic bound on accuracy of battery state and parameter estimation, J. Electrochem. Soc. 162 (9) (2015) A1879.
[51] Alexander P. Schmidt, Matthias Bitzer, Árpád W. Imre, Lino Guzzella, Experiment-driven electrochemical modeling and systematic parameterization for a lithium-ion battery cell, J. Power Sources 195 (15) (2010) 5071–5080.
[52] Ziyou Song, Jun Hou, Heath F. Hofmann, Xinfan Lin, Jing Sun, Parameter identification and maximum power estimation of battery/supercapacitor hybrid energy storage system based on cramer–rao bound analysis, IEEE Trans. Power Electron. 34 (5) (2018) 4831–4843.
[53] Chang-Hui Chen, Ferran Brosa Planella, Kieran O'Regan, Dominika Gastol, W. Dhammika Widanage, Emma Kendrick, Development of experimental techniques for parameterization of multi-scale lithium-ion battery models, J. Electrochem. Soc. 167 (8) (2020) 080534.
[54] Shichang Ma, Bingxiang Sun, Xiaojia Su, Weige Zhang, Haijun Ruan, Sensitivity analysis of electrochemical model parameters for lithium-ion batteries on terminal voltages and anode lithium plating criterion, J. Energy Storage 71 (2023) 108127.
[55] Thomas R. B. Grandjean, Liuying Li, Maria Ximena Odio, Widanalage D. Widanage, Global sensitivity analysis of the single particle lithium-ion battery model with electrolyte, in: 2019 IEEE Vehicle Power and Propulsion Conference, VPPC, IEEE, 2019, pp. 1–7.
[56] Clément Edouard, Martin Petit, Julien Bernard, Christophe Forgez, Renaud Revel, Sensitivity analysis of an electrochemical model of Li-ion batteries and consequences on the modeled aging mechanisms, ECS Trans. 66 (9) (2015) 37.

A novel hybrid electrochemical equivalent circuit model for online battery management systems

Cai, Chengxi

2024-10-01

Cai C, Gong Y, Fotouhi A, Auger DJ. (2024) A novel hybrid electrochemical equivalent circuit model for online battery management systems. Journal of Energy Storage, Volume 99, Part A, October 2024, Article number 113142

https://doi.org/10.1016/j.est.2024.113142